STABILIZED LEAST-SQUARES IMAGING CONDITIONS FOR COMMON-SHOT WAVE-EQUATION MIGRATION

B. Amaro, J. Schleicher, A. Novais, J. C. Costa, and L. T. Santos

email: *brunoama@gmail.com, js@ime.unicamp.br*

keywords: *Wave equation, Seismic reflection method, Image Analysis*

ABSTRACT

As it becomes increasingly important for migration methods to provide compensation for illumination and amplitude recovery, particularly, if the goal is to successfully recover a reflectivity of the medium, an imaging condition like simple crosscorrelation, which destroys the image amplitude, is unacceptable. For this reason, several alternative forms of imaging conditions have emerged in the recent past that are evaluated by the quality of the output amplitudes and artifacts produced. In this work we study a set of imaging conditions with illumination compensation. We also present new stabilized least-squares image conditions and compare them to previously proposed forms. Our numerical experiments on a simple horizontal interface model using a vertically inhomogeneous velocity model and on the Marmousi data set show that they produce satisfactory results. The general observation from the overall comparison is that the stabilized total least-squares imaging condition produced the best image with the least migration artifacts and the least affected migration amplitudes. Its image quality comes very close to the one of the simple crosscorrelation imaging condition, however with correctly recovered relative amplitudes.

INTRODUCTION

In wave equation migration, a fundamental step, after propagation of both source and receiver wavefields down into the subsurface model, is the application of an imaging condition. This condition decides whether a given image point is a reflector point. If correctly chosen, the imaging condition can provide additional information about the reflection coefficient. The theoretical imaging condition of Claerbout (1971) consists of dividing the upcoming wavefield by the downgoing wavefields in the frequency domain and summing the result over all frequencies and sources used in the process. Because we do not know the real reflector position in advance, this division must be carried out at all image points. This procedure causes instability, because the downgoing wavefield will be close to zero at certain points off the reflector.

To overcome this problem, many different techniques have been proposed. The first idea is to use a crosscorrelation instead of the theoretically required deconvolution (Claerbout, 1971). This procedure is perfectly stable, because no division is required. However, it destroys the amplitude information contained in the data. Therefore, many recent publications attempt to approximate the deconvolutional imaging condition in order to recover the reflection coefficient at the image point (Valenciano and Biondi, 2003; Guitton et al., 2007; Chattopadhyay and McMechan, 2008; Schleicher et al., 2008; Vivas et al., 2009).

The most successful of these approximations are the ones based on a least-squares solution of the governing equation that states that the upgoing wavefield at a reflection point is the reflection coefficient times the downgoing wavefield (Arienti et al., 2002). In its most basic form, the least-squares imaging condition (LSIC) consists of dividing the crosscorrelation of the upcoming and downgoing wavefields by the autocorrelation of the downgoing wavefield. Schleicher et al. (2006, 2007, 2008) demonstrated that two basic modifications help to further stabilize the LSIC. These are adding a small constant to the denominator (which corresponds to damped least squares), or smoothing the autocorrelation in the denominator, which

is a small modification of the original idea of Guitton et al. (2007), who proposed to smooth the absolute value of the downgoing wavefield in the denominator.

Based on the same ideas, Vivas et al. (2009) proposed to use all available shots when applying least squares. The resulting LSIC then involves the sum over all sources before the division of the correlated wavefields. To further stabilize the division, Vivas et al. (2009) replace the denominator at points of low value by a proportion of its average value. They demonstrate that this procedure further suppresses migration artifacts, but do not discuss the consequences on migration amplitudes

In this paper we combine the ideas of Vivas et al. (2009) stabilized LSICs with the stabilization techniques used in Schleicher et al. (2008). Moreover, we discuss a new set of LSICs, where the standard least-squares procedure is replaced by total least squares, combined with the same ideas of stabilization. We test all resulting LSICs on two synthetic data sets. The first model, which consists of a constant vertical velocity gradient and four horizontal interfaces, was designed to allow for amplitude evaluation. The second is the Marmousi data set, which allows a better evaluation of migration artifacts.

THEORY

Wave-equation migration tries to undo the effects that the wave propagation had on the surface data $Q(x_r, y_r; \omega)$ recorded at the receiver position $\mathbf{x}_r = (x_r, y_r, z = 0)$. These effects are generally approximately described by the acoustic wave equation which, after Fourier transform, is given by

$$\left(\frac{\omega^2}{\upsilon^2(\mathbf{x})} + \frac{\partial^2}{\partial x^2} + \frac{\partial^2}{\partial y^2} + \frac{\partial^2}{\partial z^2} \right) P(\mathbf{x}, \omega; \mathbf{x}_s) = -\delta(\mathbf{x} - \mathbf{x}_s), \tag{1}$$

where $P(\mathbf{x}, \omega; \mathbf{x}_s)$ is the wavefield at a point $\mathbf{x} = (x, y, z)$, $\upsilon(\mathbf{x})$ is the wavefield velocity, and $\mathbf{x}_s$ denotes the source position. The solution of this equation at $\mathbf{x}_r$ must be equal the recorded surface data $Q(x_r, y_r, \omega; \mathbf{x}_s)$, i.e, the wavefield $P(x_r, y_r, z = 0, \omega; \mathbf{x}_s)$ must satisfy the boundary condition

$$P(x_r, y_r, z = 0, \omega; \mathbf{x}_s) = Q(x_r, y_r, \omega; \mathbf{x}_s). \tag{2}$$

To migrate the data $Q(x_r, y_r, \omega; \mathbf{x}_s)$ means to map this solution into depth. The downward propagation is carried out in two steps. The first step propagates the upcoming field P_U back into the subsurface, starting from its registered values Q and $t = t_{max}$. Thus, this step uses the initial condition $P_U(x, y, z = 0, \omega; \mathbf{x}_s) = Q(x, y, \omega; \mathbf{x}_s)$. The other step consists of simulating a downgoing source wavefield P_D starting at the source position $\mathbf{x}_s$, i.e., with initial condition $P_D(x, y, z = 0, \omega; \mathbf{x}_s) = \delta(\mathbf{x} - \mathbf{x}_s)$. For this propagation, equation (1) can be used itself, leading to reverse-time migration (RTM), or decomposed into two one-way equations, then known as wave-equation migration (WEM).

Imaging Condition

After the propagation step, an imaging condition must be applied to obtain the migrated image. Theoretically, the correct imaging condition is the deconvolution (division in the frequency domain) of both wavefields at reflector depth to recover the reflection coefficient as the amplitude of the obtained image (Claerbout, 1971),

$$R(\mathbf{x}; \mathbf{x}_s) = \sum_{\omega} \frac{P_U(\mathbf{x}, \omega; \mathbf{x}_s)}{P_D(\mathbf{x}, \omega; \mathbf{x}_s)}. \tag{3}$$

Here and below, the symbol Σ denotes an average, i.e., it includes the division by the total number of terms. Because the reflector position is unknown, this division must be carried out at all image points. This implies a certain instability during the process, because the downgoing wavefield, which is in the denominator of equation (3), will be zero at points that are not part of a reflector. For this reason, it is necessary to find a way to stabilize the imaging process. Some ideas are described below.

Crosscorrelation. The simplest and most stable imaging condition is the one proposed by Claerbout (1971). It uses a simple crosscorrelation of the upcoming and downgoing wavefields, i.e., a convolution of the upcoming wavefield with the complex conjugate of the downgoing wavefield,

$$R_c(\mathbf{x}) = \sum_{\mathbf{x}_s} \sum_{\omega} P_U(\mathbf{x}, \omega; \mathbf{x}_s) P_D^*(\mathbf{x}, \omega; \mathbf{x}_s), \tag{4}$$

where the asterisk denotes the complex conjugate. Differently from the preceding reports of Schleicher et al. (2006, 2007), we explicitly include the sum over all sources, which completes the construction of the final image, in the expressions for all image conditions. Condition (4) is a simplification of the expression

$$R(\mathbf{x}) = \sum_{\mathbf{x}_s} \sum_{\omega} \frac{P_U(\mathbf{x}, \omega; \mathbf{x}_s) P_D^*(\mathbf{x}, \omega; \mathbf{x}_s)}{P_D(\mathbf{x}, \omega; \mathbf{x}_s) P_D^*(\mathbf{x}, \omega; \mathbf{x}_s)}, \tag{5}$$

which is obtained from equation (3) by multiplication of numerator and denominator with $P_D^*(\mathbf{x}, \omega; \mathbf{x}_s)$, an operation which moves all phase operations in the numerator and makes the denominator real.

Equation (5) does not solve the problem of division by zero. The advantage is that the denominator is now only a scale factor that does not contain any phase information, i.e., information about the reflector position. Thus, if our interest is to know the reflector position with no amplitude preservation, the denominator can be omitted, leading to imaging condition (4). The fact that imaging condition (4) does not need any division makes it the most stable and thus the most-used of all imaging conditions. On the other hand, removing a theoretically required factor means that R_c will only correctly recover the phase information, but not provide correct amplitudes.

Least-squares imaging conditions

In the following, we will discuss better approximations to equation (5) that preserve the migration amplitude. All of the imaging conditions discussed here can be interpreted as the result of least-squares inversions of the equation

$$P_U(\mathbf{x}, \omega; \mathbf{x}_s) = R(\mathbf{x}, \omega) P_D(\mathbf{x}, \omega; \mathbf{x}_s), \tag{6}$$

which governs the reflection process.

Division by autocorrelation. The most basic of these least-squares imaging conditions (LSICs), first derived by Arienti et al. (2002), is given by

$$R_{da}(\mathbf{x}) = \sum_{\mathbf{x}_s} \frac{\sum_\omega P_U(\mathbf{x}, \omega; \mathbf{x}_s) P_D^*(\mathbf{x}, \omega; \mathbf{x}_s)}{\sum_\omega P_D(\mathbf{x}, \omega; \mathbf{x}_s) P_D^*(\mathbf{x}, \omega; \mathbf{x}_s)} = \sum_{\mathbf{x}_s} \frac{\langle P_U, P_D \rangle}{\|P_D\|^2}, \tag{7}$$

where $\langle A, B \rangle = \sum_\omega A(\mathbf{x}, \omega; \mathbf{x}_s) B^*(\mathbf{x}, \omega; \mathbf{x}_s)$, and $\|A\|^2 = \langle A, A \rangle$. This imaging condition is also known as illumination compensation and can be interpreted as the result of a standard least-squares inversion of equation (6) for all frequencies, one source at a time. Other interpretations were discussed by Schleicher et al. (2008), who also addressed how to stabilize imaging condition (7). Here, we include two of the stabilization techniques discussed there, now incorporating the sum over the sources. The first one is

$$R_{daz}(\mathbf{x}) = \sum_{\mathbf{x}_s} \widehat{R}_{daz}(\mathbf{x}; \mathbf{x}_s), \quad \text{with} \quad \widehat{R}_{daz}(\mathbf{x}; \mathbf{x}_s) = \begin{cases} \dfrac{\langle P_U, P_D \rangle}{\|P_D\|^2}, & \|P_D\| > \varepsilon, \\ 0 & \text{otherwise}, \end{cases} \tag{8}$$

where

$$\varepsilon = \varepsilon(z) = \max\{\alpha, \lambda \max_{x,y} \|P_D\|\}, \tag{9}$$

and λ and α are parameters that keep ε from getting too small. The second technique is

$$R_{das}(\mathbf{x}) = \sum_{\mathbf{x}_s} \frac{\langle P_U, P_D \rangle}{\langle\!\langle \, \|P_D\|^2 \, \rangle\!\rangle}, \tag{10}$$

where

$$\langle\!\langle \, C(x_i, y_k, z; \mathbf{x}_s) \, \rangle\!\rangle = \sum_{l=i-n_x}^{i+n_x} \sum_{m=k-n_y}^{k+n_y} C(x_l, y_m, z; \mathbf{x}_s) \tag{11}$$

represents the smoothing operator proposed by Guitton et al. (2007), with n_x and n_y denoting the smoothing window sizes in the x and y directions, respectively. Another common stabilization of condition (7) uses the addition of a small positive perturbation to $\|P_D\|^2$ (damped least squares). Our numerical experiments adding ε from equation (9) yielded results that were virtually identical to those obtained by equation (8). Thus, we prefer the form (8), since it does not alter the value of the reflection coefficient.

Total least-squares. Our first new stabilization technique is based on using total least squares, which considers the errors in both P_D and P_U, instead of standard least squares, which allows errors only in P_D. The resulting imaging condition reads

$$R_{tls}(\mathbf{x}) = \sum_{\mathbf{x}_s} \frac{\langle P_U, P_D \rangle}{|\langle P_U, P_D \rangle|} \frac{\|P_U\|}{\|P_D\|}. \tag{12}$$

Equation (12) allows for a physical explanation. The two factors inside the sum over all sources are separately taking care of the kinematic (correlation over its absolute value) and dynamic (upgoing over downgoing amplitude) information. Of course, equation (12) still contains wavefield information in the denominator, which may be zero at certain image points. This can be remedied using the same stabilization techniques as before, i.e.,

$$R_{rtlzz}(\mathbf{x}) = \sum_{\mathbf{x}_s} \widehat{R}_{rtlsz}(\mathbf{x};\mathbf{x}_s), \quad \text{with} \quad \widehat{R}_{rtlsz}(\mathbf{x};\mathbf{x}_s) = \begin{cases} \dfrac{\langle P_U, P_D \rangle}{|\langle P_U, P_D \rangle|} \dfrac{\|P_U\|}{\|P_D\|}, & |\langle P_U, P_D \rangle| \, \|P_D\| > \varepsilon, \\ 0 & \text{otherwise,} \end{cases} \tag{13}$$

and

$$R_{tlss}(\mathbf{x}) = \sum_{\mathbf{x}_s} \frac{\langle P_U, P_D \rangle \, \|P_U\|}{\langle\!\langle \, |\langle P_U, P_D \rangle| \, \|P_D\| \, \rangle\!\rangle}, \tag{14}$$

where ε is defined equivalently to equation (9) and "$\langle\!\langle \cdot \rangle\!\rangle$" is the smoothing operator of equation (11).

Generalized least squares. Unlike in the imaging conditions discussed above, Vivas et al. (2009) proposed to apply least-squares inversion of equation (6) not for one source at a time, but for all sources simultaneously. This yields

$$R_{gls}(\mathbf{x}) = \frac{\sum_{\mathbf{x}_s} \langle P_U, P_D \rangle}{\sum_{\mathbf{x}_s} \|P_D\|^2}, \tag{15}$$

where the sum over all sources is carried out for numerator and denominator independently. Since even this denominator can be zero at times, condition (15) still needs stabilization. Vivas et al. (2009) propose to use a fraction of the mean energy of the downgoing field to define a threshold for the denominator. Wherever the downgoing energy is below this threshold, it is replaced by the threshold value itself. The stabilized value of the denominator is then obtained by a final sum over frequency and sources, for each spatial position.

The average of the energy of the downgoing wavefield is given by

$$M(z,\omega;\mathbf{x}_s) = \Big[\sum_{x,y} |P_D(\mathbf{x},w;\mathbf{x}_s)|^2 \Big]^{1/2}. \tag{16}$$

Using this value, Vivas et al. (2009) propose to replace the field in the denominator of equation (15) by

$$S(\mathbf{x},\omega;\mathbf{x}_s) = \max \Big\{ |P_D(\mathbf{x},\omega;\mathbf{x}_s)|, \beta M(z,\omega;\mathbf{x}_s) \Big\}, \tag{17}$$

with β an arbitrary positive constant. This defines the stabilized least-squares imaging condition given by

$$R_{sls}(\mathbf{x}) = \frac{\sum_{\mathbf{x}_s} \langle P_U, P_D \rangle}{\sum_{\mathbf{x}_s} \|S\|^2}. \tag{18}$$

Of course, the imaging condition (15) can also be stabilized using the ideas explained earlier. Below, we will thus also test the alternative conditions

$$R_{lsz}(\mathbf{x}) = \begin{cases} \dfrac{\sum_{\mathbf{x}_s} \langle P_U, P_D \rangle}{\sum_{\mathbf{x}_s} \|P_D\|^2}, & \sum_{\mathbf{x}_s} \|P_D\|^2 > \varepsilon, \\ 0 & \text{otherwise,} \end{cases} \tag{19}$$

and

$$R_{lss}(\mathbf{x}) = \frac{\sum_{\mathbf{x}_s} \langle P_U, P_D \rangle}{\langle\!\langle \sum_{\mathbf{x}_s} \|P_D\|^2 \, \rangle\!\rangle}. \tag{20}$$

Generalized total least squares. Finally, also total least-squares inversion can be applied using all sources simultaneously, leading to

$$R_{stls}(\mathbf{x}) = \frac{\sum_{\mathbf{x}_s} \langle P_U, P_D \rangle \ \|P_U\|}{\sum_{\mathbf{x}_s} |\langle P_U, P_D \rangle| \ \|P_D\|}, \tag{21}$$

which, using the same stabilization ideas, gives rise to the imaging conditions

$$R_{stlsz}(\mathbf{x}; \mathbf{x}_s) = \begin{cases} \dfrac{\sum_{\mathbf{x}_s} \langle P_U, P_D \rangle \ \|P_U\|}{\sum_{\mathbf{x}_s} |\langle P_U, P_D \rangle| \ \|P_D\|}, & \sum_{\mathbf{x}_s} |\langle P_U, P_D \rangle| \ \|P_D\| > \varepsilon, \\ 0 & \text{otherwise}, \end{cases} \tag{22}$$

and

$$R_{tslss}(\mathbf{x}) = \frac{\sum_{\mathbf{x}_s} \langle P_U, P_D \rangle \ \|P_U\|}{\langle\!\langle \sum_{\mathbf{x}_s} |\langle P_U, P_D \rangle| \ \|P_D\| \rangle\!\rangle}. \tag{23}$$

NUMERICAL EXPERIMENTS

For simplicity, the numerical experiments were carried out in two dimensions. We tested the above imaging conditions on two synthetic data sets, the first from a simple horizontally layered model, and the second being the Marmousi data set. The employed migration was phase-shift plus interpolation (PSPI) migration with ten reference velocities, chosen according to the maximum entropy criterion of Bagaini et al. (1995). Note that the same migration technique was applied in all examples, and all migrations used the true velocity distribution. The only varying parameter is the employed imaging condition. Thus, all differences between the following figures can directly be attributed to the variation of the imaging conditions.

Horizontal interfaces

To control the quality of the amplitude in the numerical experiments, the first tests were carried out using a simple model with four horizontal reflectors in a vertically inhomogeneous background model with a constant vertical gradient of 0.3/s and initial value 2000 m/s at the surface. The four reflectors were created by density contrasts in such a way that the reflection coefficients are identical, and transmission loss was neglected. Therefore, ideally, all migrated amplitudes should coincide.

For all tested imaging conditions, we show the migrated image and the amplitudes along the four reflectors. The amplitudes along the first, second, third, and fourth reflector are depicted as blue solid, green dashed, red dash-dotted, and black dotted curves, respectively.

Crosscorrelation. Figure 1 shows the results of imaging condition R_c [equation (4)]. We immediately note the different amplitudes at the different reflectors. This is a consequence of omitting the denominator. As we will see below, all other tested imaging conditions provide much better calibration between reflectors at different depths. The great advantage of this simple imaging condition is that it is virtually free of migration artifacts. The clean image of Figure 1 should be considered a benchmark for any imaging condition that includes illumination compensation.

Division by autocorrelation. Divisional imaging conditions tend to create migration artifacts. This becomes immediately clear when comparing Figure 1 with Figures 2-4, which show the results of imaging conditions R_{da}, R_{daz} and R_{das} [equations (7), (8) and (10)]. For condition R_{daz}, we found $\lambda = 10^{-3}$ and $\alpha = 10^{-6}$ in equation (9) to provide the best image. Note that all LSICs tested here provide much cleaner images than alternative conditions not based on least squares as tested in Chattopadhyay and McMechan (2008) and Schleicher et al. (2008). The migration artifacts appear only close to the surface and in the boundary zone of the image. The amplitude graphs of Figures 2-4 show that these imaging conditions achieve perfect amplitude calibration of the four reflectors in the central zone of the image, independently of the stabilization technique employed.

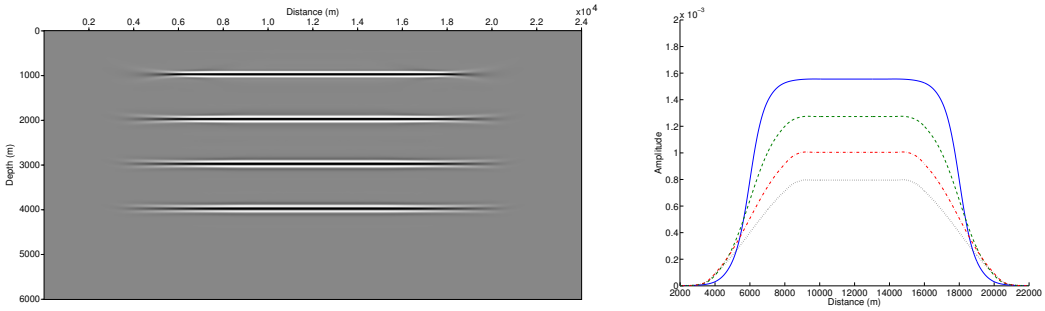

Figure 1: Left: Image using condition R_c [equation (4)]. Right: Amplitude along reflector images.

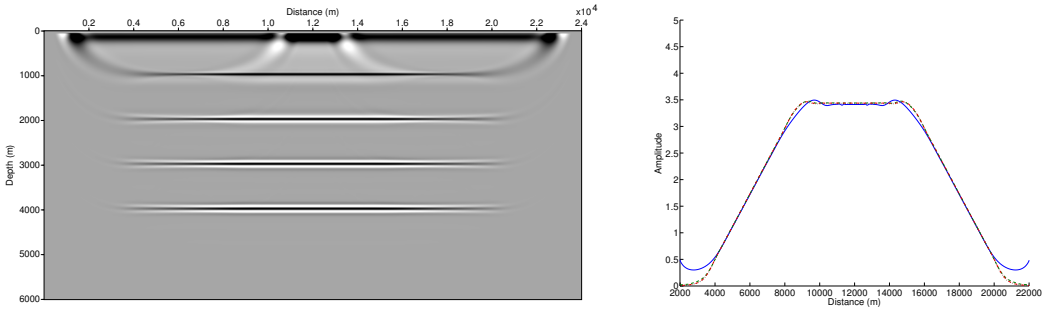

Figure 2: Left: Image using condition R_{da} [equation (7)]. Right: Amplitude along reflector images.

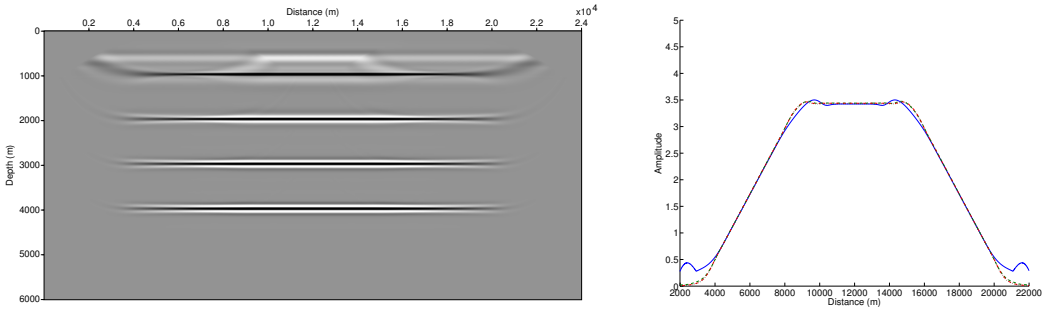

Figure 3: Left: Image using condition R_{daz} [equation (8)]. Right: Amplitude along reflector images.

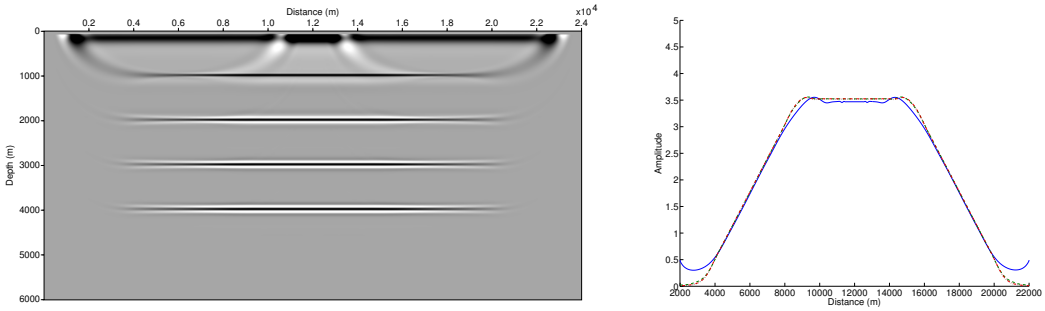

Figure 4: Left: Image using condition R_{das} [equation (10)]. Right: Amplitude along reflector images.

Total least-squares. Figures 5-7 show the results of imaging conditions R_{tls}, R_{tlsz} and R_{tlss} [equations (12), (13) and (14), respectively]. Again, after several numerical tests, we chose $\lambda = 10^{-3}$ and $\alpha = 10^{-6}$ in equation (9). The images of Figures 5-7 are very similar to Figures 2-4 for the previous set of imaging conditions. Likewise, there is no significant difference between the amplitudes over the four reflectors, except for a small difference affecting only the topmost reflector in Figure 7.

Generalized least-squares. Figures 8 and 9 show the results of imaging conditions R_{gls} and R_{sls} [equations (15) and (18)]. Several tests with different values for the number of points in equation (16) and β in equation (17) led to the choice of 275 points and $\beta = 1$. Comparing the images of Figures 8 and 9

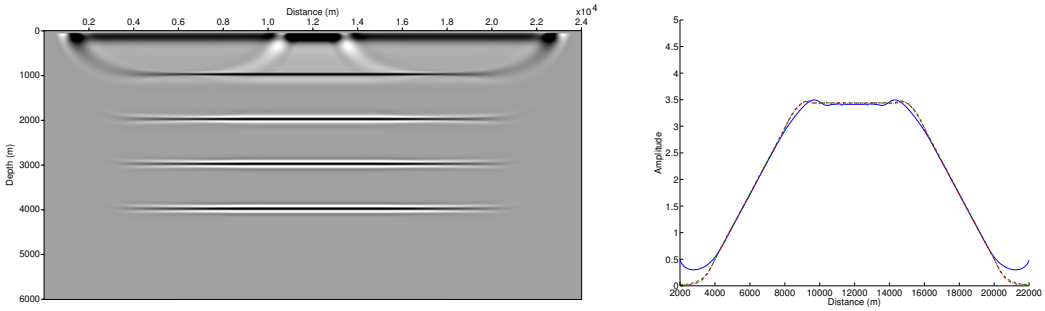

Figure 5: Left: Image using condition R_{tls} [equation (12)]. Right: Amplitude along reflector images.

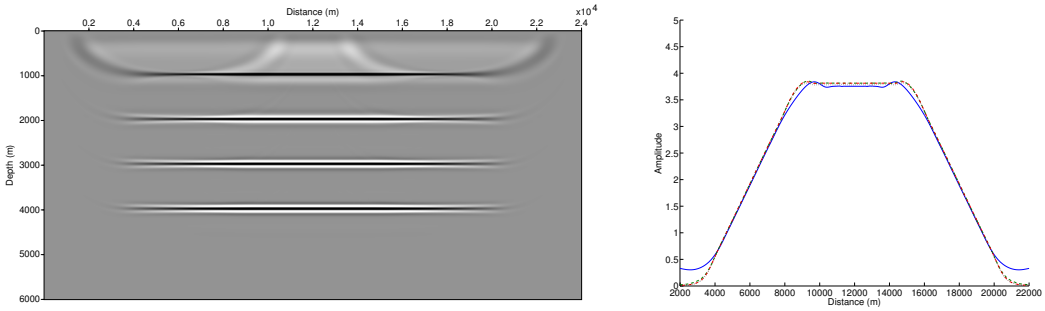

Figure 6: Left: Image using condition R_{tls} [equation (12)]. Right: Amplitude along reflector images.

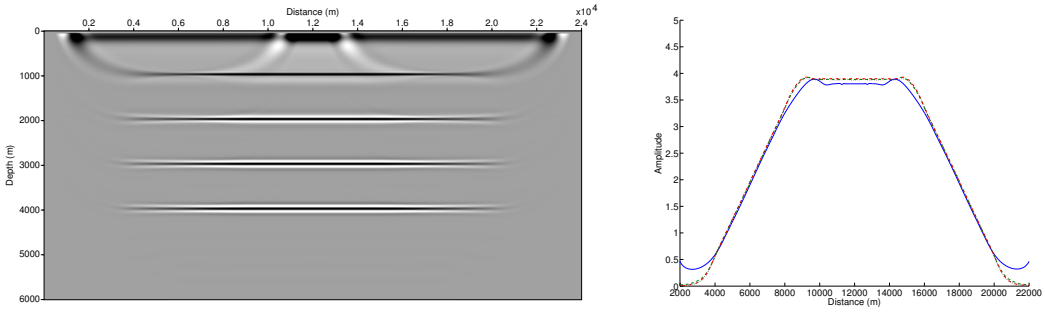

Figure 7: Left: Image using condition R_{tlss} [equation (14)]. Right: Amplitude along reflector images.

to the previous ones, we see that the aspect of the migration artifacts has changed. Now, the artifacts are completely located in the boundary zone. The stabilized version (Figure 9) even reduces these artifacts in comparison to Figure 8, confirming the observation of Vivas et al. (2009) that this imaging condition provides the cleanest images, coming close to the clean crosscorrelation image of Figure 1.

However, there is a downside to these imaging conditions. When looking at the amplitude graphs in Figures 8 and 9, we see that the reflector amplitudes are not completely calibrated, and even not constant along each individual reflector. Still, the stabilized version in Figure 9 is better than the basic one in Figure 8, but the amplitude quality is reduced in comparison to Figures 2 to 7.

The above LSICs were proposed and partly tested in previous works (Schleicher et al., 2006, 2007, 2008; Vivas et al., 2009). The next test involves the new combination of the source-sum stabilization with the more common techniques of zeroing the result if the denominator is too small [equation (19)] and smoothing the denominator [equation (20)]. We see that R_{lsz} (best result with ϵ and α as before, Figure 10) further removes the migration artifacts in the boundary zone. On the other hand, R_{lss} (best result with $n_x = 100$, Figure 11) yields a very similar result to Figures 8 and 9, The reflector amplitudes, however, are still uncalibrated for both conditions, independently of the chosen parameters.

Generalized total least squares. The fact that the generalized LSICs have produced nice images with very few artifacts has motivated us to combine the source-sum stabilization also with the total LSICs [equations (21), (22), and (23)]. The image quality of the combined imaging conditions (Figures 12-14) is comparable to the corresponding images of the generalized LSICs (Figures 8, 10, and 11). The migra-

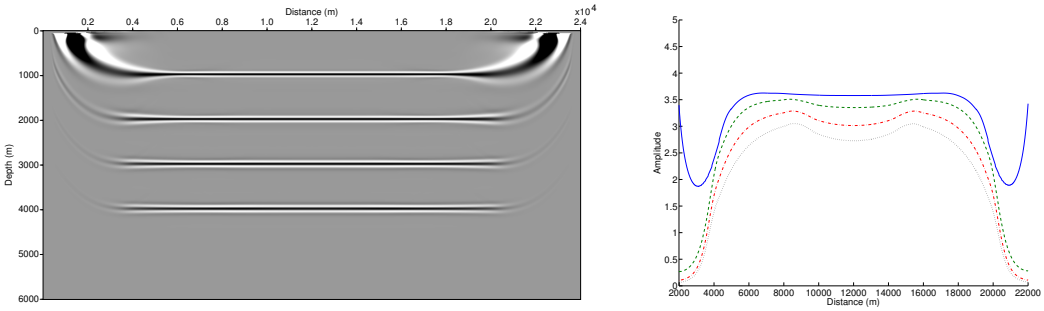

Figure 8: Left: Image using condition R_{gls} [equation (15)]. Right: Amplitude along reflector images.

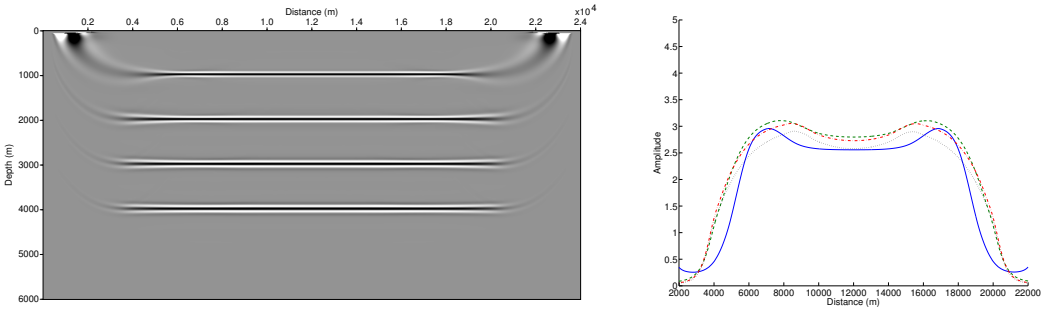

Figure 9: Left: Image using condition R_{sls} [equation (18)]. Right: Amplitude along reflector images.

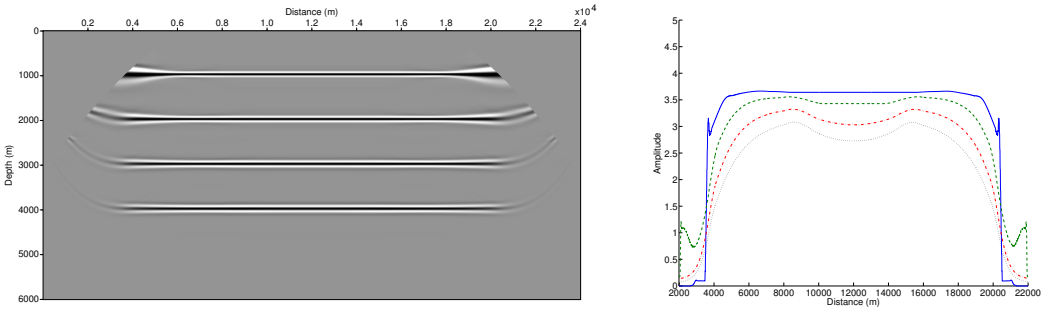

Figure 10: Left: Image using condition R_{lsz} [equation (19)]. Right: Amplitude along reflector images.

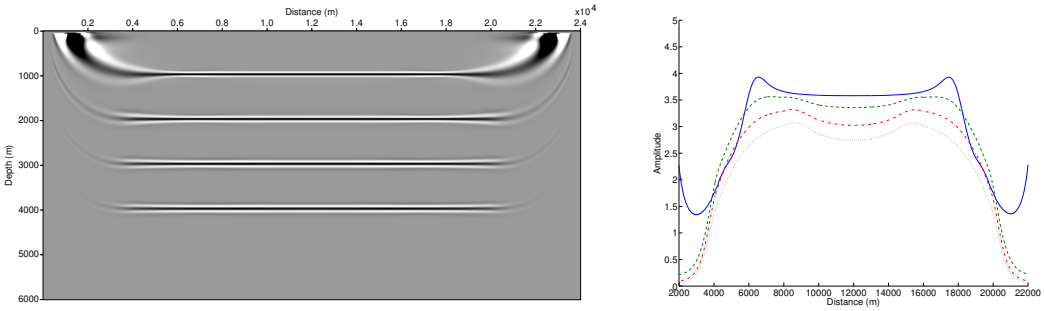

Figure 11: Left: Image using condition R_{lss} [equation (20)]. Right: Amplitude along reflector images.

tion artifacts occur in the boundary zone and are stronger than the ones in Figure 9 with the stabilization condition of Vivas et al. (2009). However, the advantage of the generalized total LSIC is the amplitude calibration. As we can see in the amplitude plots of Figures 12-14, the four reflectors' amplitudes are very well aligned. Though the are not as perfectly matched as in the LSICs of Figures 2-7, the lateral range is much wider than in these conditions.

This set of numerical experiments indicates that condition (22) is the most advantageous one, since it calibrates the amplitudes very well and removes most of the artifacts (Figure 13), coming in image quality very close to the simple crosscorrelation imaging condition of Figure 1.

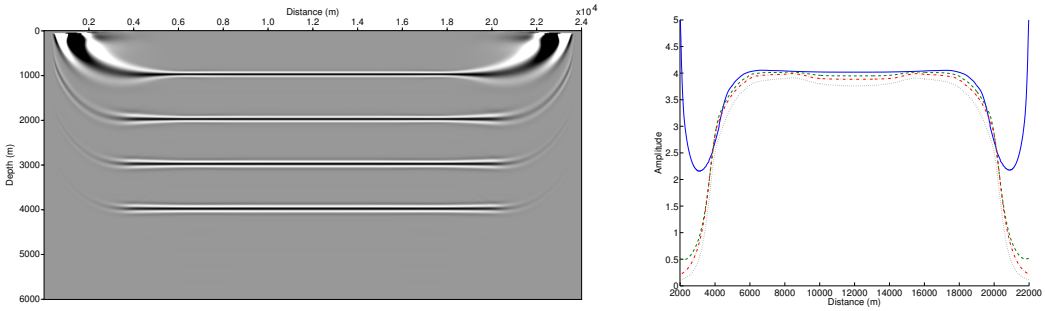

Figure 12: Left: Image using condition R_{stls} [equation (21)]. Right: Amplitude along reflector images.

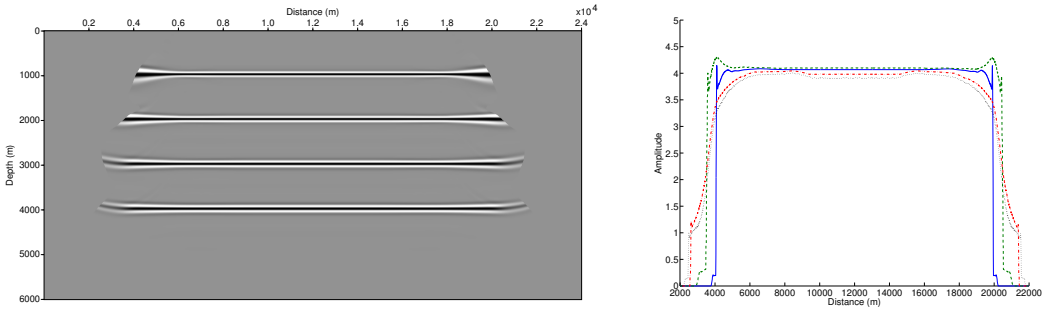

Figure 13: Left: Image using condition R_{stlsz} [equation (22)]. Right: Amplitude along reflector images.

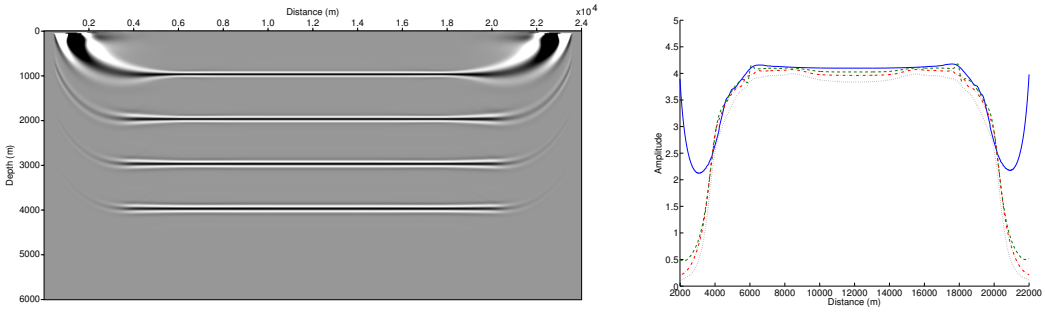

Figure 14: Left: Image using condition R_{stlss} [equation (23)]. Right: Amplitude along reflector images.

Marmousi data

To study the quality of the best of the above imaging conditions in a more realistic setting, we applied them to the Marmousi data (Versteeg, 1994). For all images below, we used the same common-shot phase-shift plus interpolation (PSPI) migration with ten reference velocities chosen according to the maximum entropy criterion of Bagaini et al. (1995). Therefore, all differences in the images below are a direct consequence of the imaging conditions used.

Crosscorrelation. Figure 15 shows the benchmark result of condition R_c, which is free of migration artifacts from deconvolution. All other imaging conditions are not supposed to degrade the image quality in comparison with this one. Note, however, that this image condition does not recover correct amplitudes, i.e., dynamic information to distinguish strong and weak reflectors is lost. Using it, shallow reflectors will always look stronger than deeper ones.

Division by autocorrelation. All following LSICs do a better job in amplitude preservation than the crosscorrelation imaging condition. We see in Figure 16 that the top-of-salt and top-of-reservoir reflectors are stronger than in Figure 15, while the sedimentary reflections in the shallow parts are reduced. However, the unconditional application of R_{da} according to equation (7) (not shown here) produces quite some artifacts. After stabilization according to equation (8) with $\lambda = 0.05$ and $\alpha = 10^{-6}$ (Figure 16) or denominator smoothing according to equation (10) with $n_x = 100$ (Figure 17), it produced much less

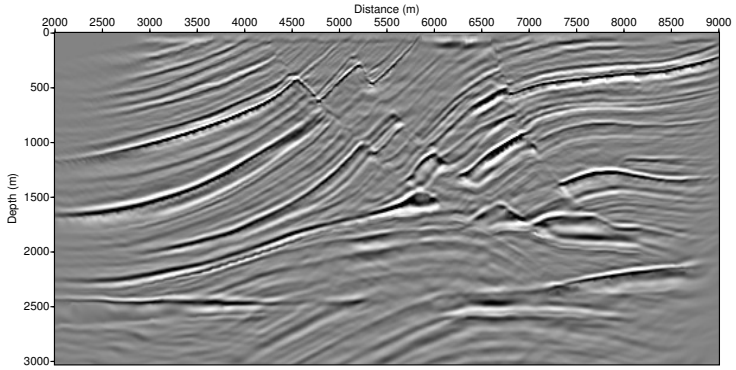

Figure 15: Marmousi data migrated using the imaging condition R_c [equation (4)].

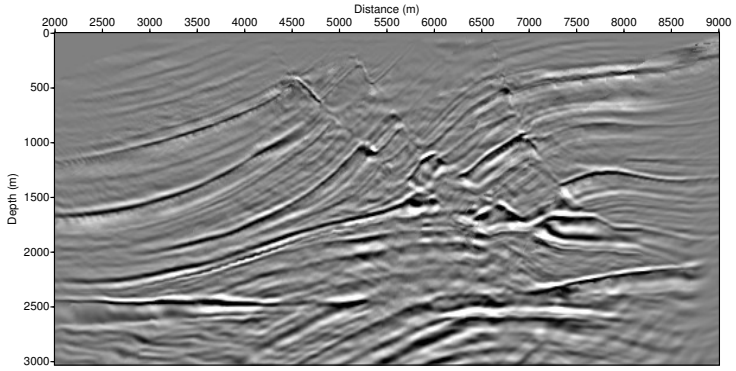

Figure 16: Marmousi data migrated using the imaging condition R_{daz} [equation (8)].

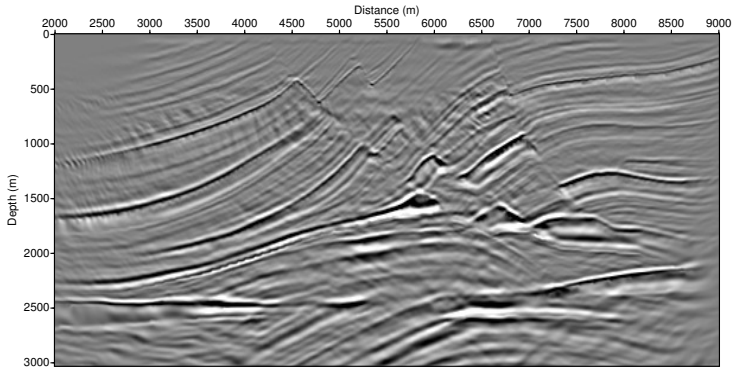

Figure 17: Marmousi data migrated using the imaging condition R_{das} [equation (10)].

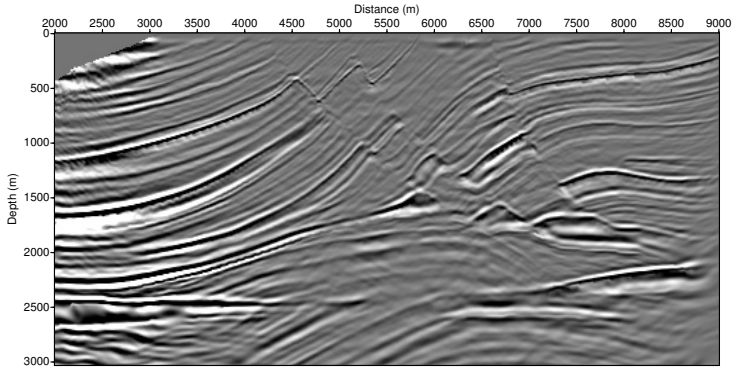

Figure 18: Marmousi data migrated using the imaging condition R_{tlsz} [equation (13)].

artifacts. Although the overall quality of both images is similar, imaging condition R_{daz} is better in the lower part of the image and R_{das} produces a clearer image in the upper part.

Total least-squares. Similar to imaging condition R_{da}, the original total LSIC R_{tls} [equation (12)] was unstable. However, the stabilized total LSICs R_{tlsz} and R_{tlss} [equations (13) and (14)] produced satisfactory results (Figures 18 and 19). Again, best results were obtained with $\lambda = 0.05$ and $\alpha = 10^{-6}$ for R_{tlsz} and $n_x = 100$ for R_{tlss}.

Comparing Figures 18 and 19 with Figures 16 and 17, which use the same stabilization techniques, we can see that several of the migration artifacts are reduced by the total LSICs R_{tlsz} and R_{tlss} (Figures 18 and 19). the images, except for In Figure 18, we recognize strongly enhanced amplitudes at the left border, which is a mixed blessing. On one hand, it allows to follow reflectors farther into the boundary zone, bu onn the other hand, artifacts are enhanced, too. Some reflectors are more enhanced in Figure 18 at the top of the image while Figure 19 presents a clearer picture on the bottom. In both cases, artifacts persist near the surface.

Generalized least-squares. The images in Figures 20 and 21 show the results of conditions R_{gls} and R_{sls}, given by equations (15) and (18), respectively. In equation (18), we obtained best results with $\beta = 1$, and in equation (9), we used $\varepsilon = 10^{-6}$. We note that in also in these figures, amplitudes are increased on the left side, where the images extend further into the border zone. After a more detailed inspection of the image in Figure 20, we see the presence of artifacts in the top left corner, a problem solved by imaging condition R_{sls} (Figure 21). However, these artifacts appear only in the boundary region of the image, where the available data are insufficient. In both cases the artifacts persist to a depth of about 1500 m.

The next subset of images (Figures 22 and 23) corresponds to the source-sum stabilized conditions R_{lsz} and R_{lss}, [equations (19) and (20)]. The most adequate parameter values for α, λ and n_x where the same as before. The resulting images are very similar to Figures 20 and 21, except that the high amplitudes close to the left border are a little reduced in Figure 22.

Generalized total least squares. Finally, Figures 24-26 show the new generalized total LSICs R_{stls}, R_{stlsz}, and R_{stlss} [equations (21), (22) and (23)]. Again, $\lambda = 0.05$, $\alpha = 10^{-6}$ produced the best results for R_{stlsz}. The best smoothing window for R_{stlss} was now $n_x = 25$.

Both R_{stlsz} and R_{stlss} show a considerable improvement over R_{sls} (Figure 22). In the case of R_{stlsz} we see a clearer top of the image compared to R_{stlss}. In general, few migration artifacts are visible in both images, particularly in Figure 25. These conditions also extend the image towards the borders like R_{gls} and R_{sls}. Therefore, we conclude that these new LSICs have acted positively, creating improved results that combine the advantages of the conditions discussed by Schleicher et al. (2008) and Vivas et al. (2009).

The general observation from the overall comparison of Figures 15 to 26 is that the stabilized total LSIC R_{stlsz} [equation (22)] produced the best image (Figure 25). Except for the region close to the left border, its image quality comes very close to the one of the simple crosscorrelation imaging condition R_c (Figure 15), however with correctly recovered relative amplitudes.

CONCLUSIONS

When the amplitudes of a migrated image are to be interpreted, the standard crosscorrelation imaging condition of Claerbout (1971) cannot be used, since it treats the amplitude information incorrectly. This is particularly important, if true-amplitude wave-propagation algorithms are used to correct for geometrical-spreading effects in heterogeneous media (Zhang et al., 2005, 2007; Amazonas et al., 2010).

Several techniques to preserve the meaning of migrated amplitudes as proportional to the reflection coefficient at the image point while avoiding problems with divisions by near-zero values have been discussed in the recent past (Valenciano and Biondi, 2003; Guitton et al., 2007; Chattopadhyay and McMechan, 2008; Schleicher et al., 2008; Vivas et al., 2009). In this paper, we have combined ideas of several of them to come up with new stabilization techniques for least-squares imaging conditions. These stabilized least-squares imaging conditions help to avoid instability problems in the migrated image.

First numerical tests on synthetic data from a horizontally layered model and on the Marmousi data indicated that the new stabilized least-squares imaging conditions can help to reduce migration artifacts. In

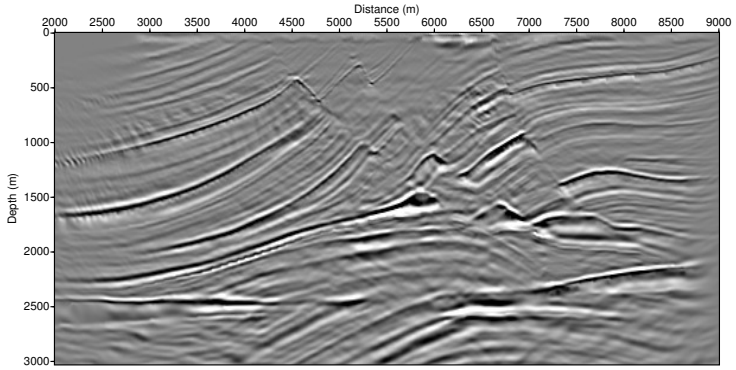

Figure 19: Marmousi data migrated using the imaging condition R_{tlss} [equation (14)].

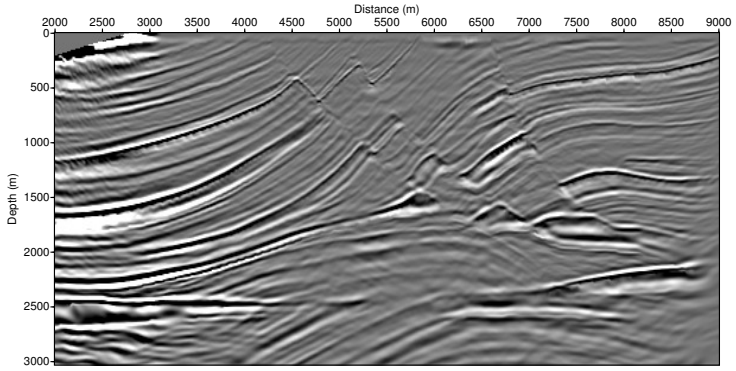

Figure 20: Marmousi data migrated using the imaging condition R_{gls} [equation (15)].

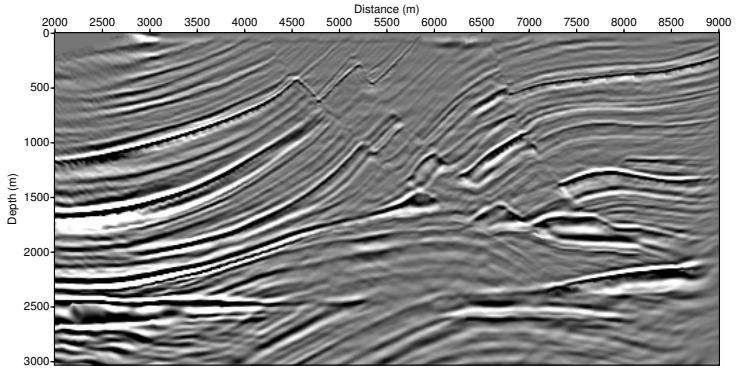

Figure 21: Marmousi data migrated using the imaging condition R_{sls} [equation (18)].

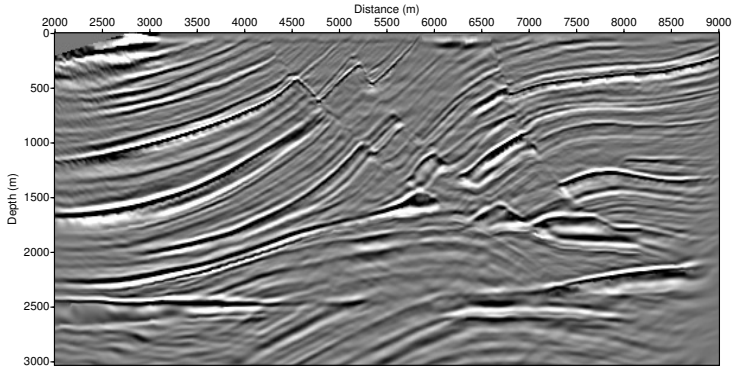

Figure 22: Marmousi data migrated using the imaging condition R_{lsz} [equation (19)].

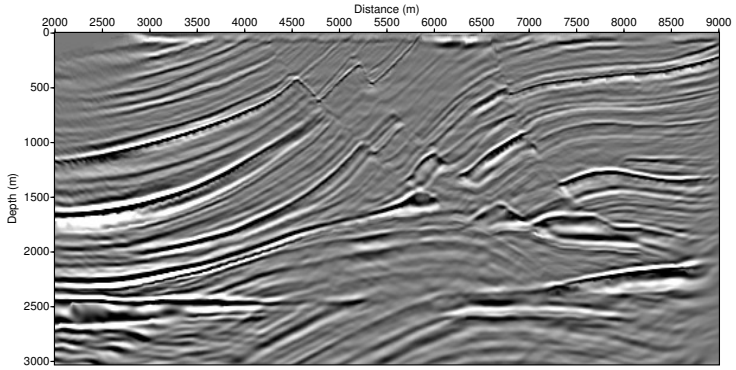

Figure 23: Marmousi data migrated using the imaging condition R_{lss} [equation (20)].

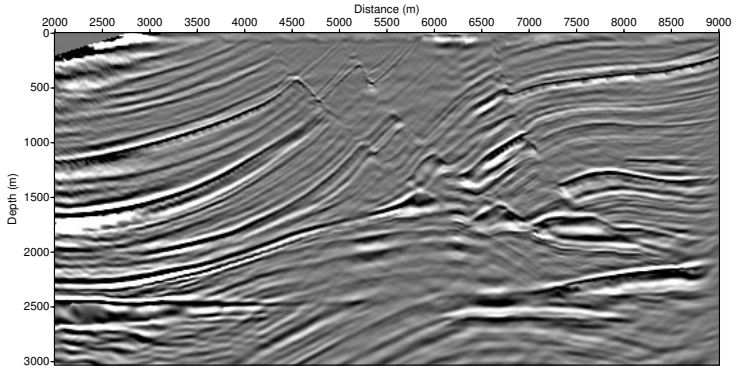

Figure 24: Marmousi data migrated using the imaging condition R_{stls} [equation (21)].

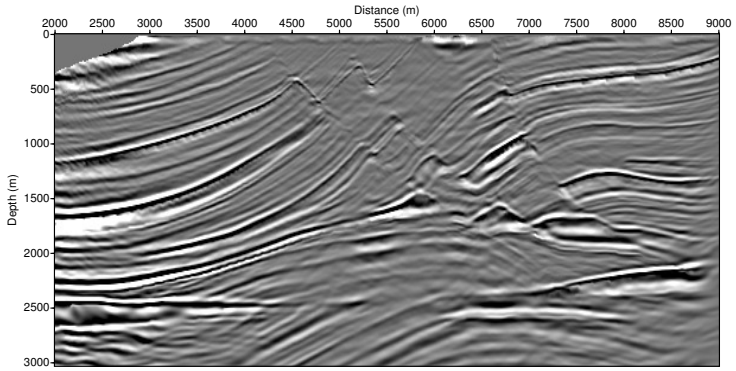

Figure 25: Marmousi data migrated using the imaging condition R_{stlsz} [equation (22)].

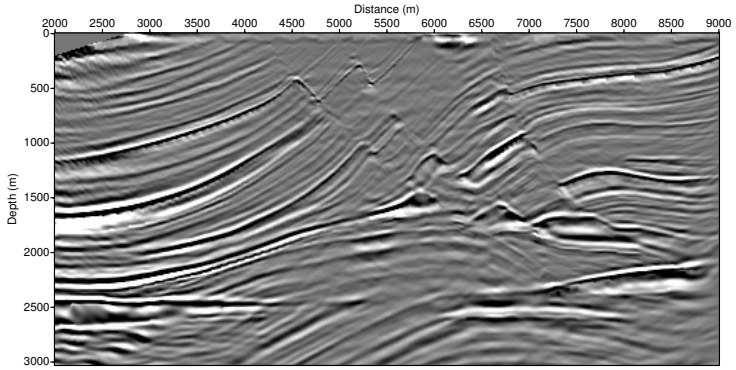

Figure 26: Marmousi data migrated using the imaging condition R_{stlss} [equation (23)].

our experiments, the new conditions resulted in superior image quality as compared to other recently proposed imaging conditions, both with regard to migration artifacts and to migrated amplitudes. Particularly, the stabilized total least-square imaging conditions not only delivered clearer images with less migration artifacts, but also preserved the relative amplitude over an extended offset.

The general observation from the overall comparison made is that the generalized total least-squares imaging condition which attributes zero where the downgoing wavefield is less than a threshold value produced the best image with the least migration artifacts and the least affected migration amplitudes. Its image quality comes very close to the one of the standard crosscorrelation imaging condition, however with correctly recovered relative amplitudes.

ACKNOWLEDGEMENTS

We would like to thank the Brazilian Research Agencies CAPES and CNPq, as well as Petrobras and the sponsors of the Wave Inversion Technology (WIT) consortium for providing financial support for this research.

REFERENCES

Amazonas, D., Aleixo, R., Schleicher, J., and Costa, J. C. (2010). Anisotropic complex Padé hybrid finite-difference depth migration. *Geophysics*, 75(2):S51–S59.

Arienti, M. T., Bonomi, E., Cardone, G., and Cazzola, L. (2002). Amplitude-preserving Monte Carlo 3D prestack migration. *64th EAGE, Conference and Exhibition, Expanded Abstracts*, B09:1–4.

Bagaini, C., Bonomi, E., and Pieroni, E. (1995). Split convolutional approach to 3D depth extrapolation:. *65th Annual International Meeting, SEG, Expanded Abstracts*, pages 195–198.

Chattopadhyay, S. and McMechan, G. A. (2008). Imaging conditions for prestack reverse-time migration. *Geophysics*, 73(3):S81–S89.

Claerbout, J. F. (1971). Toward a unified theory of reflector mapping. *Geophysics*, 36:467–481.

Guitton, A., Valenciano, A., Bevc, D., and Claerbout, J. (2007). Smoothing imaging condition for shot profile migration. *Geophysics*, 72:S149–S154.

Schleicher, J., Costa, J. C., and Novais, A. (2006). A comparison of imaging conditions for wave-equation shot-profile migration. *Annual WIT Report*, 10:118–130.

Schleicher, J., Costa, J. C., and Novais, A. (2007). Comparison of imaging conditions: Application to Marmousi data. *Annual WIT Report*, 11:163–177.

Schleicher, J., Costa, J. C., and Novais, A. (2008). A comparison of imaging conditions for wave-equation shot-profile migration. *Geophysics*, 73(6):S219–S227.

Valenciano, A. and Biondi, B. (2003). 2D deconvolution imaging condition for shot profile migration. *73rd Annual International Meeting, SEG, Expanded Abstracts*, pages 1059–1062.

Versteeg, R. (1994). The Marmousi experience: Velocity model determination on a synthetic complex data set:. *The Leading Edge*, 13:927–936.

Vivas, F. A., Pestana, R. C., and Ursin, B. (2009). A new stabilized least-squares imaging condition:. *Journal of Geophysics and Engineering*, 6:264–268.

Zhang, Y., Xu, S., Bleistein, N., and Zhang, G. (2007). True-amplitude, angle-domain, common-image gathers from one-way wave-equation migrations. *Geophysics*, 72(1):S49–S58.

Zhang, Y., Zhang, G., and Bleistein, N. (2005). Theory of true-amplitude one-way wave equations and true-amplitude common-shot migration. *Geophysics*, 70(4):E1–E10.